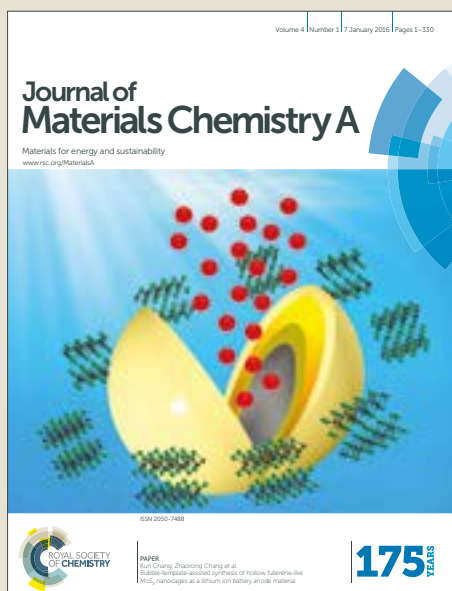


# Journal of Materials Chemistry A

Accepted Manuscript



This article can be cited before page numbers have been issued, to do this please use: E. Luo, M. Xiao, J. Ge, C. Liu and W. Xing, *J. Mater. Chem. A*, 2017, DOI: 10.1039/C7TA07608H.



This is an Accepted Manuscript, which has been through the Royal Society of Chemistry peer review process and has been accepted for publication.

Accepted Manuscripts are published online shortly after acceptance, before technical editing, formatting and proof reading. Using this free service, authors can make their results available to the community, in citable form, before we publish the edited article. We will replace this Accepted Manuscript with the edited and formatted Advance Article as soon as it is available.

You can find more information about Accepted Manuscripts in the [author guidelines](#).

Please note that technical editing may introduce minor changes to the text and/or graphics, which may alter content. The journal's standard [Terms & Conditions](#) and the ethical guidelines, outlined in our [author and reviewer resource centre](#), still apply. In no event shall the Royal Society of Chemistry be held responsible for any errors or omissions in this Accepted Manuscript or any consequences arising from the use of any information it contains.



Journal Name

ARTICLE

## Selectively doping pyridinic and pyrrolic nitrogen into 3D porous carbon matrix through template-induced edge engineering: enhanced catalytic activity towards oxygen reduction reaction

Ergui Luo,<sup>abc</sup> Meiling Xiao,<sup>ac</sup> Junjie Ge,<sup>\*ac</sup> Changpeng Liu<sup>\*ac</sup> and Wei Xing<sup>\*acd</sup>Received 00th January 20xx,  
Accepted 00th January 20xx

DOI: 10.1039/x0xx00000x

www.rsc.org/

Developing cost-effective and highly efficient oxygen reduction electrocatalysts, such as non-precious metal and metal-free catalysts, is undoubtedly crucial for the commercialization of low-temperature fuel cells. Here, edge-rich nitrogen doped porous carbon catalyst for oxygen reduction reaction (ORR) with high proportion of pyridinic and pyrrolic N (up to 94%) was synthesized by an in-situ released CO<sub>2</sub> activation method, using glucose and melamine as precursors, nano-CaCO<sub>3</sub> as template. The catalysts exhibit three-dimensional structure, hierarchical pores and large pore volumes. Benefiting from the increased active site density and structural advantage, the optimized catalyst shows excellent ORR activity with half-wave potential of 0.853 V and long-term stability in alkaline media, which is among the best in all reported metal-free catalysts.

### Introduction

The lack of high-performance and low-cost electrocatalysts for the sluggish oxygen reduction reaction (ORR) is still the main obstacle for the wide commercial application of fuel cells.<sup>1-3</sup> Currently, platinum and its alloys are remain as the most efficient ORR catalysts, which suffer severely from the problems including scarcity, high-cost and poor stability.<sup>4,5</sup> Extensive studies have been conducted to search for non-precious metal<sup>2, 3, 6-8</sup> and metal-free<sup>9-13</sup> alternatives to noble metal catalysts for ORR. Among metal-free catalysts, nitrogen-doped carbon materials have attracted much attention owing to their intrinsic low cost, superior electrical conductivity, excellent durability, and environmental friendliness.<sup>14-17</sup> It has been confirmed by both experimental studies<sup>9,15</sup> and theoretical calculations<sup>18-20</sup> that the ORR activity of nitrogen-doped carbon materials is originated from the charge delocalization of the carbon atoms due to nitrogen incorporation, which facilitates oxygen adsorption and reduction. The activity was reported to be highly dependent on the doping level and types of nitrogen atoms. Previous studies revealed that pyridinic N and pyrrolic N with planar

structures are always located on exposed edge planes and are more active towards ORR.<sup>21-24</sup> Recently, Wei and co-workers synthesized nitrogen-doped graphene with high yield of planar N using a space-confinement method as a metal-free catalyst which manifested outstanding ORR activities.<sup>21</sup> However, the reported strategy for the preferred formation of planar N species was time-consuming and complicated, which is not suitable for large-scale production. Apart from nitrogen species, the pore structure of nitrogen-doped carbon catalyst is another critical factor in fuel cells. Interconnected hierarchical pores are believed to promote the mass transportation, resulting in enhanced ORR activity.<sup>17, 25-27</sup> To date, it remains a great challenge to develop suitable strategies to maximize the exposure of active nitrogen atoms as well as optimize the porosity of carbon matrix.

In this work, we present the design and fabrication of nitrogen-doped carbon materials with high yield of pyridinic and pyrrolic N, as efficient metal-free ORR electrocatalysts. The ultrathin nanosheets assembled sponge-like nitrogen-doped porous carbon (denoted as SNPC-X, where X represents the pyrolysis temperature (°C)) was obtained through simple carbonization of a mixture of melamine and glucose with nano-CaCO<sub>3</sub> acting as template (Scheme S1). Layered graphitic carbon nitride (g-C<sub>3</sub>N<sub>4</sub>) was formed during the pyrolysis of melamine, which acted as a sacrificial template to direct the formation of carbon nanosheets.<sup>28</sup> In addition, CO<sub>2</sub> released from thermal decomposition of hard template contributed to the exposure of more edges and efficient utilization of nitrogen atoms (see the following XPS analysis).<sup>29</sup> This synthetic strategy avoided cumbersome processes and costly raw materials, making it potentially applicable towards the facile fabrication of high-performance N-doped carbon-based ORR catalysts.

<sup>a</sup> Laboratory of Advanced Power Sources, Changchun Institute of Applied Chemistry, Chinese Academy of Sciences, Changchun, Jilin, 130022, PR China. E-mail: liuchp@ciac.ac.cn, gejj@ciac.ac.cn; Fax: +86-431-85685653; Tel: 86-431-85262223

<sup>b</sup> University of Science and Technology of China, Hefei, Anhui, 230026, PR China

<sup>c</sup> Jilin Province Key Laboratory of Low Carbon Chemical Power Sources, Changchun, Jilin, 130022, PR China

<sup>d</sup> State Key Laboratory of Electroanalytical Chemistry, Changchun Institute of Applied Chemistry, Chinese Academy of Sciences, Changchun, Jilin, 130022, PR China. E-mail: xingwei@ciac.ac.cn

† Footnotes relating to the title and/or authors should appear here.

Electronic Supplementary Information (ESI) available: [details of any supplementary information available should be included here]. See DOI: 10.1039/x0xx00000x

## Experimental

### Chemicals and materials

a-D-Glucose was purchased from Beijing Chemical Works. Nano-CaCO<sub>3</sub> (40-80 nm) was provided by Nanjing XFNano Company. High-purity potassium hydroxide and melamine were purchased from Aladdin Company. 5 wt% Nafion ionomer was obtained from Sigma-Aldrich. Commercial state-of-the-art 20 wt% Pt/C (Johnson Matthey Company, HiSPEC 3000) was used as the benchmark for comparison. Ethanol and HCl were purchased from Beijing Chemical Works. All the chemicals were used as delivered without further treatment. Ultrapure water (Millipore, 18.23 MΩ cm) was used throughout all experiments.

### Catalyst preparation

In a typical synthesis, nano-CaCO<sub>3</sub>, glucose and melamine with a mass ratio of 5:5:2 were first dissolved or dispersed into a mixture of ultrapure water and alcohol (volume ratio of 2:1), and stirred at room temperature for 5h. The solvents were evaporated at 85°C under vigorous stirring to obtain a homogeneous precursor. Subsequently, the composite underwent a pyrolysis and carbonization process under flowing argon at 700-1000°C for 2h with a heating rate of 5°C/min. The hard templates were leached out in diluted HCl solution for 24h to isolate N-doped porous carbon (SNPC-X). Control samples PC-X and NC-X were prepared using a similar procedure, but in the absence of melamine and template, respectively. The carbonization product of only glucose was labeled as C-X. The same pyrolysis protocol of precursors without glucose did not leave any carbonized products. The SNPC-SiO<sub>2</sub> was prepared at 900°C with silica template instead of nano-CaCO<sub>3</sub>. Silica nanoparticles (100-160 nm) were synthesized by the Stöber method<sup>30</sup>. Samples obtained at 900°C with nano-CaCO<sub>3</sub>/glucose mass ratios of 1:5 and 3:5 were labeled as SNPC-900-0.2 and SNPC-900-0.6, respectively.

### Material characterization

Scanning electron microscopy (SEM) measurements were performed with an XL 30 ESEM-FEG field emission scanning electron microscope. Transmission electron microscopy (TEM), high-angle annular dark-field scanning transmission electron microscopy (HAADF-STEM) and element mapping analysis were conducted on Philips TECNAI G2 electron microscope operating at 200 kV. Power X-ray diffraction (XRD) measurements were performed on PW1700 diffractometer (Philips Co.) with a Cu Kα (λ=0.15405 nm) radiation source operating at 40 kV and 30 mA. Raman spectra were collected on a J-Y T64000 Raman spectrometer with 514.5 nm wavelength incident laser light. The textural and morphological features of the various carbon supports and catalysts prepared were determined by nitrogen physisorption at 77 K in a Micromeritics ASAP 2020. X-ray photoelectron spectroscopy (XPS) measurements were carried out on Mg Kα radiation source (Kratos XSAM-800 spectrometer). The binding energy was calibrated against the C 1s line. Thermo gravimetric analysis (TGA) was performed with a Pyres 1 TGA apparatus (Perkin Elmer, MA), with a heating rate of 5 °C min<sup>-1</sup> from 50 to 1000 °C in Ar atmosphere.

### Electrochemical measurements

The electrochemical performances were conducted using the 750E Bipotentiostat (CH Instruments). SNPC catalyst ink was prepared by ultrasonically dispersing 5 mg of SNPC catalyst in a suspension containing 50μL Nafion (5wt%) solution and 950μL ethanol, while Pt/C catalyst (20wt% Pt on Vulcan XC-72 carbon, Johnson Matthey) ink was prepared by dispersing 5 mg catalyst ultrasonically in a mixture solution containing 50μL Nafion (5wt%) solution, 550μL isopropanol and 400μL Milli-Q water. The catalyst film coated electrode was obtained by dispersing the catalyst ink on a glassy carbon rotating disk electrode or rotating ring disk electrode followed by drying in air. The catalyst loadings on RDE and RRDE in all cases were 0.5 mg cm<sup>-2</sup> except for Pt/C (30μgPt cm<sup>-2</sup>). A conventional three-electrode cell was employed incorporating a saturated calomel electrode (SCE) as the reference electrode, a Pt foil as the counter electrode and the catalyst film coated RDE or RRDE as the working electrode.

The electrolyte was 0.1 M KOH solution for ORR test. RDE measurements were conducted by linear sweep voltammetry (LSV) from 1.1 V to 0.2 V at a scan rate of 10 mV s<sup>-1</sup> at 1600rpm, while the ring electrode of RRDE was held at 1.3 V vs. RHE. The H<sub>2</sub>O<sub>2</sub> collection coefficient at the ring in RRDE experiments was 0.37, as measured using a Fe(CN)<sub>6</sub><sup>4-/3-</sup> redox couple. All the ORR currents presented in the figures are faradaic currents, i.e. after correction for the capacitive current and have already been normalized to the electrode surface area. The following equations were used to calculate *n* (the apparent number of electrons transferred during ORR) and % H<sub>2</sub>O<sub>2</sub> (the percentage of H<sub>2</sub>O<sub>2</sub> released during ORR).

$$n = \frac{4I_D}{I_D + (I_R/N)} \quad (1)$$

$$\%H_2O_2 = 100 \frac{2I_R/N}{I_D + (I_R/N)} \quad (2)$$

where *I<sub>D</sub>* is the faradaic current at the disk, *I<sub>R</sub>* the faradaic current at the ring and *N* is the H<sub>2</sub>O<sub>2</sub> collection coefficient at the ring. The apparent number of electrons transferred for ORR was also determined by the Koutechy-Levich equation given below:

$$\frac{1}{J} = \frac{1}{J_L} + \frac{1}{J_K} = \frac{1}{B\omega^{1/2}} + \frac{1}{J_K} \quad (3)$$

$$B = 0.62nFC_0(D_0)^{2/3}\nu^{-1/6} \quad (4)$$

where *J* is the measured current density, *J<sub>K</sub>* is the kinetic current density, *J<sub>L</sub>* is the diffusion limited current density, *ω* is the electrode rotation rate, *F* is Faraday constant (96485 C mol<sup>-1</sup>), *C<sub>0</sub>* is the bulk concentration of O<sub>2</sub> (1.2×10<sup>-3</sup> mol L<sup>-1</sup>), *D<sub>0</sub>* is the diffusion coefficient of O<sub>2</sub> (1.9×10<sup>-5</sup> cm<sup>2</sup> s<sup>-1</sup>) and *ν* is the kinetic viscosity of the electrolyte (0.01 cm<sup>2</sup> s<sup>-1</sup>)<sup>31</sup>. In all figures, the potentials were converted to values versus the reversible hydrogen electrode (RHE). The conversion from SCE to RHE is done by measuring the voltage Δ*E* between the SCE and a Pt-black coated Pt wire immersed in the same electrolyte saturated with H<sub>2</sub>. The measured Δ*E* was 0.998 V in 0.1 M KOH solution. The accelerated durability tests (ADTs) were performed at room temperature in O<sub>2</sub>-saturated 0.1 M KOH solution by applying cyclic potential sweeps between 0.6 and 1.0 V versus RHE at a sweep rate of 200 mV s<sup>-1</sup> for 10000 cycles.

## Results and discussion

Representative scanning electron microscopy (SEM) and transmission electron microscopy (TEM) images at different magnifications are shown in Fig. 1, revealing the formation of sponge-like structure composed of ultrathin nanosheets and non-uniform pores of the final SNPC-900 catalyst. STEM image and associated elemental mapping image (Fig. 1f) reveal the homogeneous distribution of nitrogen element in carbon matrix.

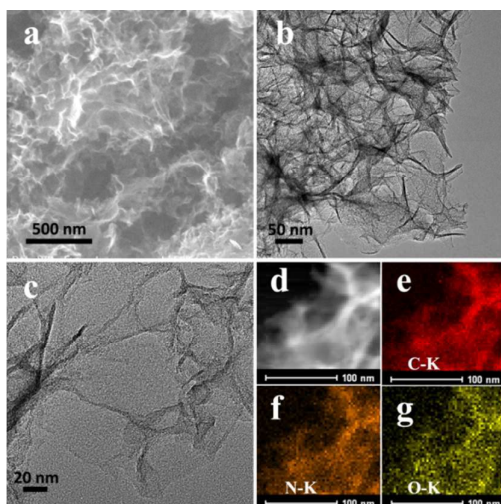


**Fig. 1** (a) SEM image; (b-c) TEM images; (d) scanning transmission microscopy (STEM) image and (e-g) elemental mappings of SNPC-900.

Nevertheless, no obvious flake structure can be observed for the C-900 and PC-900 samples (Fig. S1), indicating an indispensable role of melamine in the growth of carbon nanosheets. Furthermore, three-dimensional structure and much thinner nanosheets are found for the SNPC-900 compared with NC-900 (Fig. S1c, f), suggesting that nano-CaCO<sub>3</sub> template may prevent the nanosheets from aggregation to some extent.

We further investigate the porous structure and specific surface areas of samples by N<sub>2</sub> adsorption-desorption technique. The SNPC-900 shows a type-IV isotherm with a distinct hysteresis loop at a relative pressure  $P/P_0$  of 0.4-1 (Fig. 2a), indicating the existence of lots of mesopores. The BET specific surface area is measured to be 621.4 m<sup>2</sup>/g with total pore volume of 2.2 cm<sup>3</sup>/g. Pore size distribution analysis confirms the hierarchical porous structure with micropore (1.2 nm) by DFT method as well as meso- and macropores by BJH method (Fig. 2c-d). Specifically, the pore size distribution of SNPC-900 (20-180 nm) is much wider than particle size distribution of nano-CaCO<sub>3</sub> template (40-80 nm), which can be attributed to: i) the CaCO<sub>3</sub> template decomposition is accompanied with releasing of CO<sub>2</sub>, which further reacts with carbon atoms according to the equation: CO<sub>2</sub>+C→2CO.<sup>29</sup> This effect enlarges the pores or creates new pores; ii) some meso- and macropores come from micropores that connected up by CO<sub>2</sub> activating agent. For comparison, the NC-900 obtained without template exhibits typical type-I isotherm characteristics for only microporous materials with specific surface area of 1029 m<sup>2</sup>/g and total pore volume of 0.56 cm<sup>3</sup>/g (Fig. 2b). The pore size distribution analysis

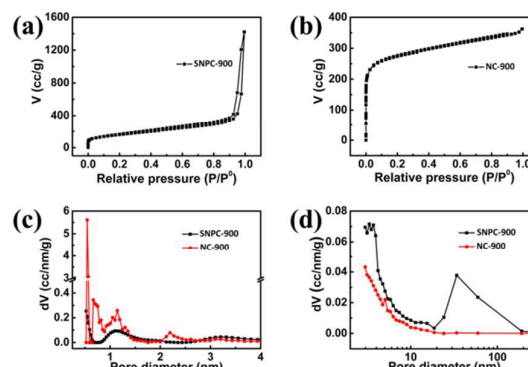


**Fig. 2** Desorption isotherms of (a) SNPC-900 and (b) NC-900 samples; The corresponding pore size distribution curves calculated from the desorption branches by utilizing (c) nonlocal density functional theory (NLDFT) and (d) Barrett-Joyner-Halenda (BJH) method.

(Fig. 2c-d) further confirms the microporosity. By introducing template, the SNPC-900 exhibits lower specific surface area but larger total pore volume than NC-900. As mentioned above, the released CO<sub>2</sub> activating gas can enlarge or connect up pores, resulting in fewer micropores in SNPC-900, which play the greatest role in evaluating specific surface area. Meanwhile, abundant meso- and macropores increase the total pore volume. All these morphology and structural features (3D structure, hierarchical pores and large pore volume) can provide SNPC-900 more contact interfaces, facilitating the transfer of electrolyte ions and electrons, thereby improving its catalytic activity.

Raman spectra (Fig. 3a) show the typical D-band at roughly 1327 cm<sup>-1</sup> and G-band at about 1586cm<sup>-1</sup>, resulting from the disordered and sp<sup>2</sup>-hybridized graphitic carbon atoms, respectively. The ratio of integrated intensities I<sub>D</sub>/I<sub>G</sub> is found to decrease with increasing pyrolysis temperature, indicating that higher degree of graphitization is obtained for SNPC-X at higher temperatures. Similar results can be obtained from the powder X-ray diffraction (XRD) patterns (Fig. 3b) with a peak at ca. 26.5° corresponding to the (002) planes of the graphitic carbon. Moreover, SNPC-900 exhibits a higher I<sub>D</sub>/I<sub>G</sub> ratio than NC-900, which can be ascribed to the increased edges in the carbon matrix.

X-ray photoelectron spectroscopy (XPS) analysis confirms the successful introduction of nitrogen atoms into the carbon-based materials (Fig. 3c). As the pyrolysis temperature increases from 700 to 1000°C, total nitrogen content of the SNPC-X reduces significantly from 10.18 at% to 2.22 at% due to the loss of unstable nitrogen (Table S1). The atomic contents of N dopant are estimated to be 5.39 at% and 2.13 at% for SNPC-900 and NC-900, respectively. Meanwhile, high resolution N 1s spectra (Fig. 3d-e) are further deconvoluted into three main signals corresponding to pyridinic N (398.2±0.1 eV), pyrrolic N (399.6±0.2 eV) and quaternary N (400.9 eV). The relative contents of quaternary N and pyridinic N increase with elevating pyrolysis temperature, whereas pyrrolic N decreases (Table S1). It is worth noting that SNPC-900 possesses a much higher percentage of pyridinic and pyrrolic N (94 %), which exhibit higher electrocatalytic activity for ORR, compared with NC-900 (44.5 %), as shown in Fig. 3d-e and Table S1, suggesting that nano-CaCO<sub>3</sub> template can effectively promote the N doping as well as alter the

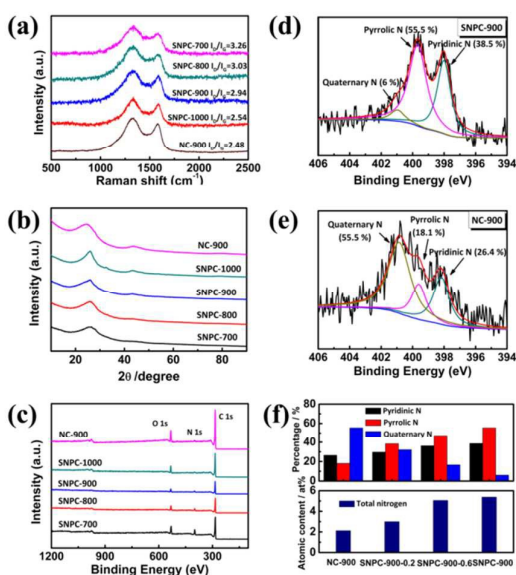
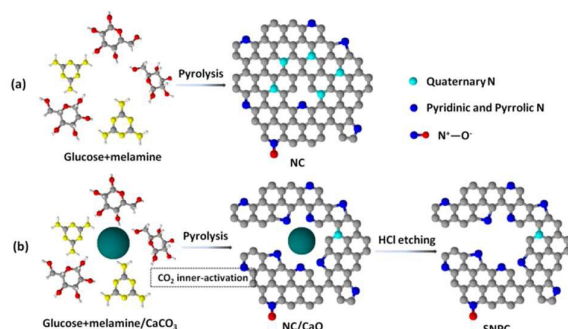


**Fig. 3** (a) Raman spectra for the different catalysts; (b) XRD patterns of each sample; (c) XPS survey spectra of different catalysts; (d-e) High resolution N 1s spectra of SNPC-900 and NC-900; (f) Total nitrogen atomic contents and N species percentages of NC-900, SNPC-900-0.2, SNPC-900-0.6 and SNPC-900.

N doping types. Considering pyridinic N and pyrrolic N are always located on exposed edge planes, we conclude that nano-CaCO<sub>3</sub> templates play an important role in promoting edge exposure, which is in consistency with the Raman analysis result mentioned above. The mechanism can also be explained by "CO<sub>2</sub> inner-activation effect". During the carbonization process, CO<sub>2</sub> gas released from CaCO<sub>3</sub> template reacted with carbon atoms during its diffusion, forming abundant exposed-edges. Nitrogen atoms were readily anchored to these defective edge sites, resulting in more pyridinic and pyrrolic N species, as illustrated in Scheme 1. Moreover, because of the loss of carbon atoms, total N doping level is elevated. Thermal gravity analysis (TGA) of nano-CaCO<sub>3</sub> and XRD pattern of carbonization product before HCl washing further confirm the decomposition of CaCO<sub>3</sub> (Fig. S2). To highlight the unique role of nano-CaCO<sub>3</sub> template, we also synthesized SNPC-SiO<sub>2</sub> with silica template instead for comparison. As anticipated, SNPC-SiO<sub>2</sub> (Fig. S3f) is observed to have almost the same N content as NC-900 and much lower percentage of pyridinic and pyrrolic N (25%). Further comparative studies were conducted on NC-900,



**Scheme 1** Schematic view revealing the selectively formation of planar edge-N in the SNPC catalyst.

SNPC-900-0.2, SNPC-900-0.6 and SNPC-900 which were prepared with different amount of nano-CaCO<sub>3</sub>. As shown in Fig. 3f, total nitrogen atomic content as well as pyridinic N and pyrrolic N percentages are positively associated with the nano-CaCO<sub>3</sub>/ glucose mass ratio, while it is opposite for the quaternary N percentage. All these results strongly reveal the critical role of nano-CaCO<sub>3</sub> template to promote the preferred formation of pyridinic and pyrrolic N.

The catalytic performance of the resulting materials towards ORR was then assessed on a three-electrode electrochemical station by rotating disk electrode (RDE) voltammetry in 0.1 M KOH solution, and compared against that of a state-of-the-art commercial Pt/C catalyst (Johnson Matthey Company, Pt/C, 20 wt%). Results are shown in Fig. 4a-b. The catalytic performances of samples in terms of half-wave potential and limiting current density are gradually enhanced by increasing the nano-CaCO<sub>3</sub>/glucose mass ratio, and all the SNPC-X catalysts show superior performances to NC-900 and SNPC-SiO<sub>2</sub>. These are ascribed to high doping levels of pyridinic and pyrrolic N species of the SNPC-Xs, thus providing sufficient reactive sites, as well as the advanced pore structures to facilitate mass transfer. Especially, the SNPC-900 manifests the most positive half-wave potential of 0.853 V, just 15mV lower than that of commercial Pt/C catalyst, and exhibits one of the highest ORR electrocatalytic activities compared with other heteroatom-doped carbon catalysts reported in the literatures<sup>32-36</sup>. However, relatively poor catalytic performance is observed for the SNPC-700 which possesses the

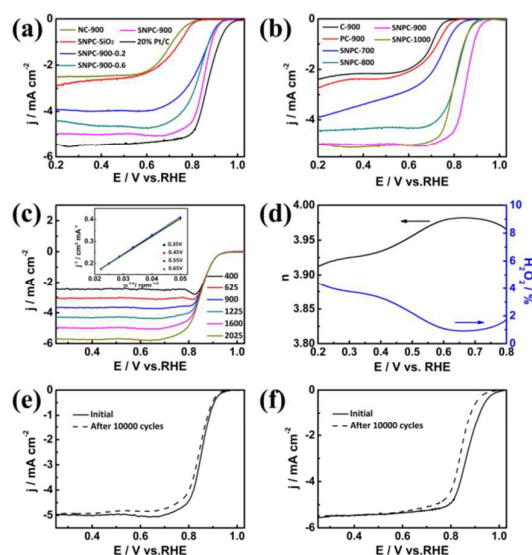


**Fig. 4** ORR performance for the synthesized catalysts. (a) RDE polarization curves of nitrogen-doped carbon catalysts prepared at 900°C and Pt/C in O<sub>2</sub>-saturated 0.1 M KOH with scan rate of 10 mV s<sup>-1</sup> and rotation speed of 1600 rpm; (b) RDE polarization curves of C-900, PC-900 and catalysts prepared at different temperatures; (c) LSVs for oxygen reduction on SNPC-900 in O<sub>2</sub>-saturated 0.1M KOH at various rotation speeds with scan rate of 10 mV s<sup>-1</sup>. Inset: K-L plots at different potentials; (d) The H<sub>2</sub>O<sub>2</sub> yielding and corresponding electron transfer number for SNPC-900 in 0.1 M KOH. ORR polarization plots of (e) SNPC-900 and (f) Pt/C before and after 10000 potential cycles in O<sub>2</sub>-saturated 0.1 M KOH.

highest N content (10.18 at%), implying the crucial importance of optimal combination of N doping level and graphitic degree. The extracted electron transfer number of SNPC-900 from the K-L plots is 3.7-3.8 (Fig. 4c). The ORR pathway is also assessed by RRDE measurement (Fig. 4d) with peroxide yield calculated to be less than 5% and n ranges from 3.9 to 4.0 at potentials ranging from 0.2 to 0.8 V, demonstrating that an apparent four-electron pathway is the dominant mechanism. Tafel slope at low over-potentials for SNPC-900 is found to be 58 mV/dec (Fig. S5), even slightly smaller than that of Pt/C catalyst (62 mV/dec), indicating similar ORR kinetics on these two catalysts and the transfer of the first electron as the rate-determining step.

An accelerated durability test protocol was carried out to evaluate the electrochemical stability of the SNPC-900 and Pt/C catalysts (Fig. 4e-f). After 10000 cycles, the half-wave potential for SNPC-900 shifts negatively by about 10 mV, much lower than that for the Pt/C catalyst (27 mV). The superb stability of SNPC-900 can be attributed to the chemical and mechanical stable carbonaceous texture and unique three-dimensionally porous structure, effectively preventing the loss of active sites and structural collapse.

## Conclusions

In summary, highly pyridinic and pyrrolic nitrogen doped porous carbon assembled of thin nanosheets was fabricated by a simple one-pot, scalable method and acted as an excellent electrocatalyst for ORR. Both melamine and template were proven to play vital roles in the formation of final carbon nanostructure. The ultrahigh doping level of planar exposed-edge N was induced by CO<sub>2</sub> activation from nano-CaCO<sub>3</sub> template. The outstanding ORR catalytic activity and superior stability were ascribed to the increased active N species and advanced pore structure, which facilitates mass transportation and prevents structural collapse. This work may give researchers great inspirations in low-cost and large-scale production of porous carbon-based catalysts for fuel cells, even extended fields of water splitting, adsorbents and supercapacitors.

## Acknowledgements

The work is supported by the National Natural Science Foundation of China (21433003, 21633008), National Science and Technology Major Project (2016YFB0101202), Jilin Province Science and Technology Development Program (20150101066JC, 20160622037JC, and 20170203003SF), Hundred Talents Program of Chinese Academy of Sciences and the Recruitment Program of Foreign Experts (WQ20122200077).

## Notes and references

- 1 M. K. Debe, *Nature*, 2012, **486**, 43-51.
- 2 G. Wu, K. L. More, C. M. Johnston and P. Zelenay, *Science*, 2011, **332**, 443-447.
- 3 Z. S. Wu, S. Yang, Y. Sun, K. Parvez, X. Feng and K. Müllen, *J. Am. Chem. Soc.*, 2012, **134**, 9082-9085.
- 4 H. A. Gasteiger, S. S. Kocha, B. Sompalli and F. T. Wagner, *Appl. Catal., B*, 2005, **56**, 9-35.

- 5 D. Yu, E. Nagelli, F. Du and L. Dai, *J. Phys. Chem. Lett.*, 2010, **1**, 2165-2173.
- 6 M. Lefevre, E. Proietti, F. Jaouen and J. P. Dodelet, *Science*, 2009, **324**, 71-74.
- 7 S. Yasuda, A. Furuya, Y. Uchibori, J. Kim and K. Murakoshi, *Adv. Funct. Mater.*, 2016, **26**, 738-744.
- 8 Y. Chang, F. Hong, C. He, Q. Zhang and J. Liu, *Adv. Mater.*, 2013, **25**, 4794-4799.
- 9 K. Gong, F. Du, Z. Xia, M. Durstock and L. Dai, *Science*, 2009, **323**, 760-764.
- 10 L. Yang, S. Jiang, Y. Zhao, L. Zhu, S. Chen, X. Wang, Q. Wu, J. Ma, Y. Ma and Z. Hu, *Angew. Chem. Int. Ed.*, 2011, **50**, 7132-7135.
- 11 Y. Su, Y. Zhang, X. Zhuang, S. Li, D. Wu, F. Zhang and X. Feng, *Carbon*, 2013, **62**, 296-301.
- 12 W.-J. Jiang, J.-S. Hu, X. Zhang, Y. Jiang, B.-B. Yu, Z.-D. Wei and L.-J. Wan, *J. Mater. Chem. A*, 2014, **2**, 10154-10160.
- 13 Z. Pei, J. Zhao, Y. Huang, Y. Huang, M. Zhu, Z. Wang, Z. Chen and C. Zhi, *J. Mater. Chem. A*, 2016, **4**, 12205-12211.
- 14 A. Fasolino, J. H. Los and M. I. Katsnelson, *Nat. Mater.*, 2007, **6**, 858-861.
- 15 W. Yang, T. P. Fellinger and M. Antonietti, *J. Am. Chem. Soc.*, 2011, **133**, 206-209.
- 16 T. Ikeda, M. Boero, S. F. Huang, K. Terakura, M. Oshima and J. Ozaki, *J. Phys. Chem. C*, 2008, **112**, 14706-14709.
- 17 Y. Chen, R. Ma, Z. Zhou, G. Liu, Y. Zhou, Q. Liu, S. Kaskel and J. Wang, *Adv. Mater. Interfaces*, 2015, **2**, 1500199.
- 18 S. Maldonado and K. J. Stevenson, *J. Phys. Chem. B*, 2005, **109**, 4707-4716.
- 19 F. Gao, G. L. Zhao, S. Yang and J. J. Spivey, *J. Am. Chem. Soc.*, 2013, **135**, 3315-3318.
- 20 L. Zhang and Z. Xia, *J. Phys. Chem. C*, 2011, **115**, 11170-11176.
- 21 W. Ding, Z. Wei, S. Chen, X. Qi, T. Yang, J. Hu, D. Wang, L. J. Wan, S. F. Alvi and L. Li, *Angew. Chem. Int. Ed.*, 2013, **52**, 11755-11759.
- 22 C. V. Rao, C. R. Cabrera and Y. Ishikawa, *J. Phys. Chem. Lett.*, 2010, **1**, 2622-2627.
- 23 J. Liu, P. Song and W. Xu, *Carbon*, 2017, **115**, 763-772.
- 24 Z. H. Sheng, L. Shao, J. J. Chen, W. J. Bao, F. B. Wang and X. H. Xia, *ACS Nano*, 2011, **5**, 4350-4358.
- 25 J. Tang, J. Liu, C. Li, Y. Li, M. O. Tade, S. Dai and Y. Yamauchi, *Angew. Chem. Int. Ed.*, 2015, **54**, 588-593.
- 26 J. Liang, X. Du, C. Gibson, X. W. Du and S. Z. Qiao, *Adv. Mater.*, 2013, **25**, 6226-6231.
- 27 W. He, C. Jiang, J. Wang and L. Lu, *Angew. Chem. Int. Ed.*, 2014, **53**, 9503-9507.
- 28 F. Liu, K. Huang, S. Ding and S. Dai, *J. Mater. Chem. A*, 2016, **4**, 14567-14571.
- 29 C. Zhao, W. Wang, Z. Yu, H. Zhang, A. Wang and Y. Yang, *J. Mater. Chem.*, 2010, **20**, 976-980.
- 30 W. Stöber, A. Fink and E. Bohn, *J. Colloid Interface Sci.*, 1968, **26**, 62-69.
- 31 S. Wang, D. Yu and L. Dai, *J. Am. Chem. Soc.*, 2011, **133**, 5182-5185.
- 32 J. Li, Y. Zhang, X. Zhang, J. Huang, J. Han, Z. Zhang, X. Han, P. Xu and B. Song, *ACS Appl. Mater. Interfaces*, 2017, **9**, 398-405.
- 33 H. W. Liang, X. Zhuang, S. Brüller, X. Feng and K. Müllen, *Nat. Commun.*, 2014, **5**, 4973.
- 34 G. Wang, Y. Sun, D. Li, H. W. Liang, R. Dong, X. Feng and K. Müllen, *Angew. Chem. Int. Ed.*, 2015, **54**, 15191-15196.
- 35 T. N. Ye, L. B. Lv, X. H. Li, M. Xu and J. S. Chen, *Angew. Chem. Int. Ed.*, 2014, **53**, 6905-6909.
- 36 Y.-N. Zhu, C.-Y. Cao, W.-J. Jiang, S.-L. Yang, J.-S. Hu, W.-G. Song and L.-J. Wan, *J. Mater. Chem. A*, 2016, **4**, 18470-18477.